Acta Oceanol. Sin., 2018, Vol. 37, No. 11, P. 8–18
DOI: 10.1007/s13131-018-1277-2
http://www.hyxb.org.cn
E-mail: hyxbe@263.net

The spatiotemporal features of submesoscale processes in the northeastern South China Sea

DONG Jihai[1]*, ZHONG Yisen[2]

[1] School of Marine Sciences, Nanjing University of Information Science and Technology, Nanjing 210044, China

[2] Institute of Oceanology, Shanghai Jiaotong University, Shanghai 200240, China

Received 29 March 2018; accepted 26 April 2018

Abstract

The spatiotemporal features of submesoscale processes (SMPs) in the northeastern South China Sea (SCS) are analyzed based on a high-resolution simulation from 2009 to 2012. The simulation results show that the SMPs with a vertical relative vorticity that matches the local planetary vorticity are ubiquitous in the upper ocean of the northeastern SCS. The SMPs distribution shows an asymmetry due to centrifugal instability, with stronger positive vorticity than negative vorticity. Meanwhile, the SMPs demonstrate an obvious seasonal variation. The SMPs are strong and active in winter but weak and inactive in summer. An investigation of the SMPs generation mechanisms reveals that flow straining and mixed layer depth account for this seasonal variation. The strong flow straining and deep mixed layer depth in winter favor the SMP generation via frontogenesis and mixed layer instability.

Key words: submesoscale processes, South China Sea, frontogenesis, mixed layer instability

Citation: Dong Jihai, Zhong Yisen. 2018. The spatiotemporal features of submesoscale processes in the northeastern South China Sea. Acta Oceanologica Sinica, 37(11): 8–18, doi: 10.1007/s13131-018-1277-2

1 Introduction

Submesoscale processes (SMPs) at scales of $O(1)$ km and $O(1)$ day have drawn increasing attention due to their dynamical and ecological effects. High-resolution model simulations and observations have recently demonstrated the prevalent distribution of the SMPs in the world oceans with the typical structures of submesoscale front, eddy and filaments (Capet et al., 2008a; Callies et al., 2015; Rosso et al., 2015; Buckingham et al., 2016; Gula et al., 2016).

The SMPs, as the intermediate processes between the mesoscale and microscale dynamics, are confirmed to play an important role in a forward energy cascade. The geostrophic turbulence is characterized by an inverse energy cascade, that is, energy transferring from smaller scale to larger scale. However, an ocean flow has a forward energy cascade, and energy transfers from larger scale to smaller scale when the SMPs emerge (Capet et al., 2008c). Therefore, the SMPs provide an essential route for the mesoscale eddy dissipation and mixing enhancement (Zhang et al., 2016; Yang et al., 2017). On the other hand, the Rossby number of the SMPs is around 1, $Ro \approx O(1)$, thus indicating that the SMPs are ageostrophic. According to the analysis of *in situ* observation and model simulation, the vertical velocity induced by the SMPs reaches O(10–100) m/d, which contributes to the marine ecology considerably (Pollard and Regier, 1992; Mahadevan et al., 2006). The upwelling of the SMPs cannot only transport nutrients into the euphotic layer for phytoplankton growth, but also bring the deep phytoplankton into surface to alleviate light limitation (Lévy et al., 2001, 2012; Lapeyre and Klein, 2006; Johnson et al., 2010). On the contrary, the downwelling exhibits a negative effect by subducting nutrients or phytoplankton into the deep ocean (Lévy et al., 2001).

Different generation mechanisms of the SMPs have been proposed under various background conditions. However, frontogenesis and mixed layer instability (MLI) have been found to be the most common mechanisms for the SMP generation in the upper ocean (e.g., Capet et al., 2008b; Mensa et al., 2013). The frontogenesis theory describes a cross-front secondary circulation accompanied by front strengthening (Hoskins, 1982), while the MLI is a type of baroclinic instability that is constrained in the upper mixed layer (Boccaletti et al., 2007). A submesoscale disturbance can grow by extracting potential energy from the unstable flow because the mixed layer is not completely well-mixed and usually has a weak horizontal density gradient.

The South China Sea (SCS) is one of the most complex marginal seas in the world, with different dynamic processes such as basin-scale circulations, mesoscale eddies, internal waves, upwelling and mixing events (Liu et al., 2008; Chen et al., 2011; Alford et al., 2015; Zhang et al., 2016; Huang et al., 2016; Xia et al., 2016; Yang et al., 2016). However, little is known about the SMPs in the SCS as only few works focus on them. Zheng et al. (2008) found submesoscale vortex trains behind Babuyan Island by using surface drifters and advanced synthetic aperture radar images; these vortex trains may have been generated from the interaction between ocean currents and the islands. Recent *in situ* ob-

Foundation item: The National Key Research and Development Program of China under contract No. 2017YFA0604103; the National Basic Research Program (973 Program) of China under contract No. 2014CB745003; the National Natural Science Foundation of China under contract No. 91628302; the Startup Foundation for the Introducing Talent of the Nanjing University of Information Science and Technology under contract No. 2243141601059.

*Corresponding author, E-mail: jihai_dong@nuist.edu.cn

servations in the SCS indicate that the SMPs are active at the periphery of mesoscale eddies and make a great contribution to the dissipation of eddies and elevated mixing (Zhang et al., 2016; Yang et al., 2017; Zhong et al., 2017). Nevertheless, the spatiotemporal features of the SMPs and the corresponding potential generation mechanisms in the SCS remain unclear. This work is aimed at investigating the spatiotemporal variation of the SMPs in the northeastern SCS through a numerical model. Section 2 reviews the model setup. Section 3 presents main results. Section 4 provides a summary of this work.

2 Model setup

The simulation is performed using the Regional Oceanic Modeling System (ROMS) (Shchepetkin and McWilliams, 2005). A two-layer nested model with a parent grid of 5 km resolution and a nested grid of 1 km resolution is used to obtain a high-resolution simulation. The model has 30 vertical layers with at least ten layers in the upper 100 m. The 5 km parent grid covers the northern SCS and the eastern Luzon Strait (the black rectangle area in Fig. 1, 15°–25°N，110°–126°E), whereas the 1 km nested grid is located at the west of the Luzon Strait (the red box in Fig. 1, 18°–23°N, 115.5°–121°E). The nested grid has a wide depth range from exceeding 5 000 m in the deep basin to tens of meters over the continental shelf. This area is considered energetic, given the occurrence of multiscale dynamical processes, such as basin-scale circulation, mesoscale eddies, and internal tides.

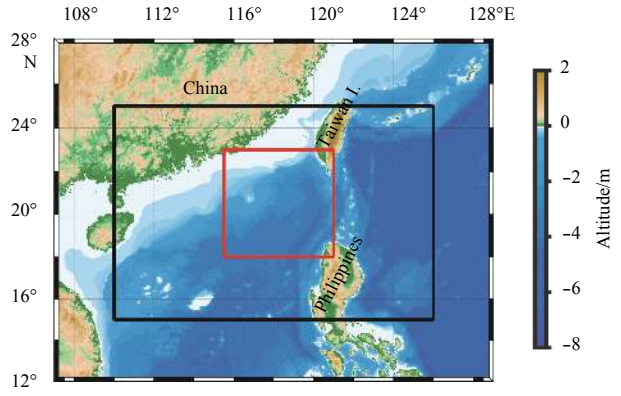

Fig. 1. The topography of model domain. The black rectangle is the parent grid with spatial resolution of 5 km, while the red one is the nested grid with spatial resolution of 1 km.

The topography used here has a spatial resolution of 2′ provided by ETOPO2. The forcing data are from the European Center for Medium-range Weather Forecasts (ECMWF) datasets with a horizontal resolution of 0.125°. The boundary condition is provided by Hybrid Coordinate Ocean Model (HYCOM) datasets with a resolution of up to 0.08°.

The parent grid first spins for 25 a using climatological forcing data to obtain a statistically stable solution. The model is then run for 9 a using monthly averaged forcing and boundary data from 2004 to 2012. Finally, the nested grid is driven from 2009 to 2012 using a one-way off-line integration on the basis of the results of the parent grid as the boundary condition.

3 Spatiotemporal variation of submesoscale processes

3.1 *The spatial variation of submesoscale processes*

The model results have revealed that various SMPs with Rossby number around $O(1)$ including fronts, filaments and eddies appear in the ocean upper layer as the model resolution increases. On the basis of the high-resolution results, a comparison of sea surface temperature is conducted between the simulation result and the satellite observation (Fig. 2). The observed sea surface temperature from December 12 to 19, 2009 is derived from the Moderate-Resolution Imaging Spectroradiometer (MODIS). The temperature is averaged with a spatial resolution of 4 km. The sea surface temperature indicates that the general patterns of the two distributions are nearly consistent. The sea surface temperature is warm in the deep basin and cold over the continental shelf. Strong temperature fronts can be found along the shelf break. However, fine differences between them are also observed. The MODIS result denotes that the front along the shelf break bends and generates meanders. However, the simulated front shows more finer structures, including filaments and eddies.

The instantaneous distributions of sea surface height, surface vertical relative vorticity (normalized by planetary vorticity, ζ/f), and horizontal density gradient ($\rho_h=(\rho_x^2+\rho_y^2)^{-1/2}$) on December 17, 2009, are illustrated in Fig. 3. The distribution of the sea surface height denotes that two mesoscale eddies with the spatial scale of $O(100)$ km can be observed in the northeastern SCS. The mesoscale eddy that is located in the west is a warm eddy with a high sea surface height of up to 0.9 m at its center, whereas the other one that is located in the east is a cold eddy with a low sea surface height below 0.4 m at its center. According to the geo-

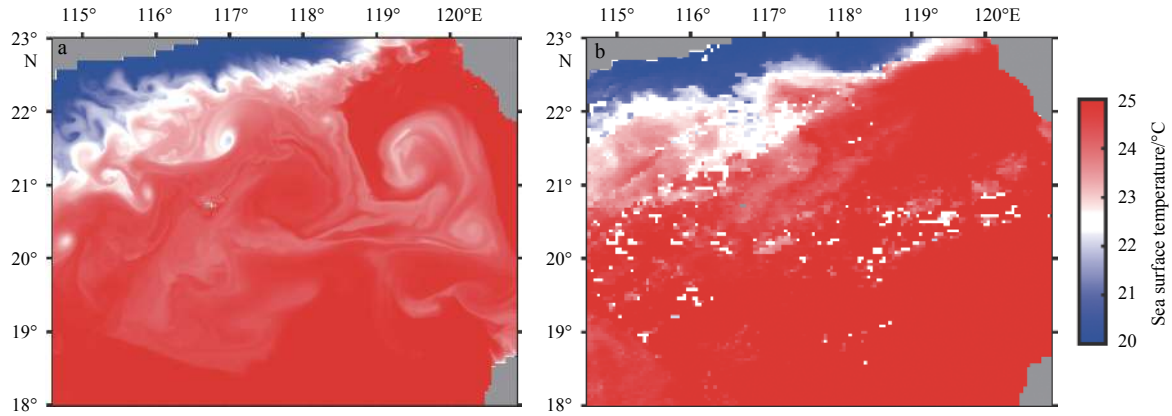

Fig. 2. The simulated sea surface temperature on December 17, 2009 (a) and 8-day averaged sea surface temperature with a spatial resolution of 4 km derived from MODIS (b).

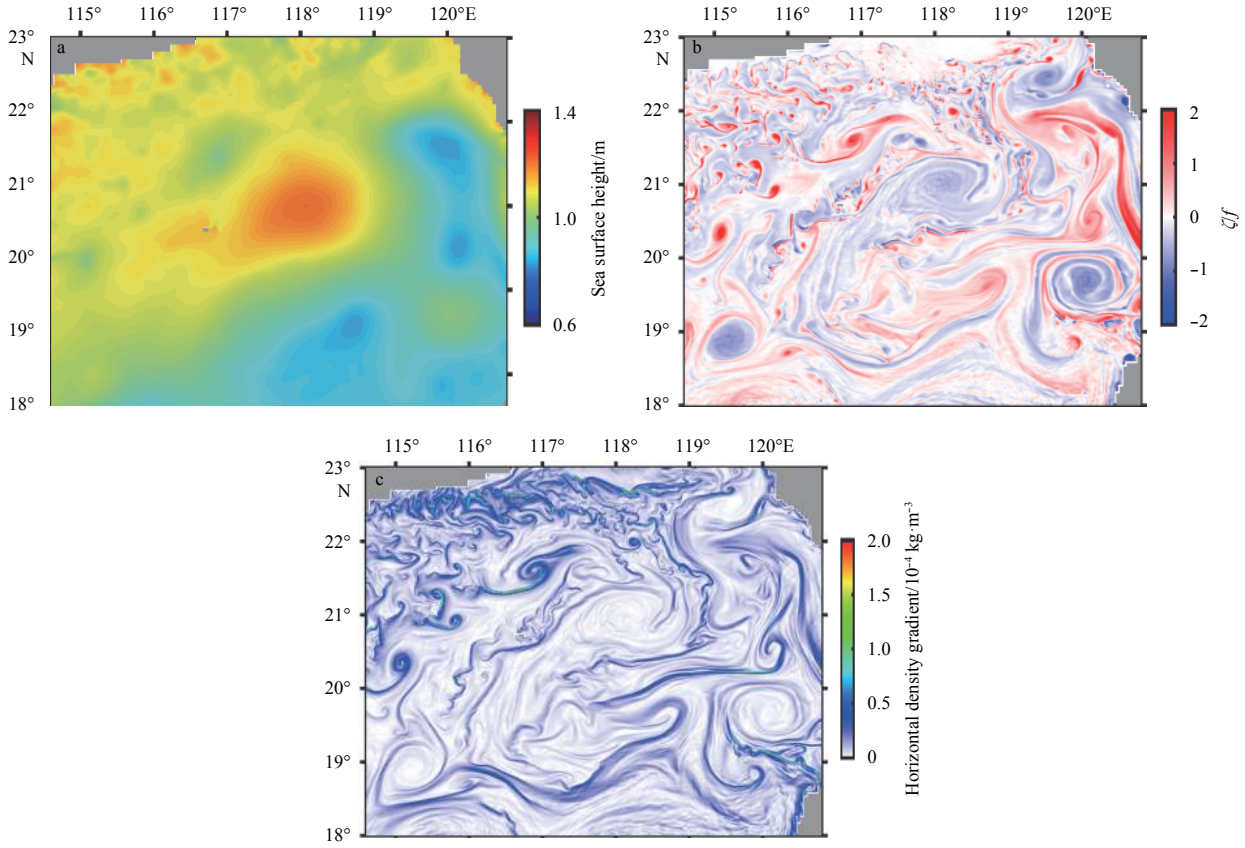

Fig. 3. The instantaneous distributions of sea surface height (a), vertical relative vorticity (ζ/f) at 5 m depth (b) and horizontal density gradient at 5 m depth (c) on December 17, 2009 from the nested 1 km grid.

strophic balance, the warm eddy has an anticyclone circulation at the surface, whereas the cold eddy exhibits a cyclone circulation (the current filed is not shown here). The two eddies, which are usually referred to as the "eddy pair", have been studied by a number of works (e.g., Zhang et al., 2013). Their generation remains an open question and different mechanisms, such as the local wind force and the Kuroshio intrusion, have been proposed (Wang et al., 2008; Nan et al., 2011; Zu et al., 2013; Shu et al., 2016; Zhang et al., 2016).

The normalized relative vorticity, which can be regarded as an expression of the Rossby number, implies the ageostrophy of the flow in the ocean. The flow tends to show ageostrophic features when the relative vorticity is comparable with the planetary vorticity. The distribution of the normalized relative vorticity at 5 m depth indicates that dynamic processes with the Rossby number that reaches $O(1)$, including filaments, eddies and fronts, are ubiquitous in the upper layer. The large magnitude of the Rossby number indicates that numerous SMPs occur in this region. The SMPs are ubiquitous in the upper layer, and they are more active in the eddy and over areas with complicated topography. Compared with the horizontal density gradient in Fig. 3c, a favorable consistency can be observed between their distributions, and a strong density gradient typically corresponds to active SMPs. This consistency, which is analyzed below, suggests a correlation between the SMPs and the density gradient.

A close examination of Fig. 3b indicates an asymmetry between the positive and negative vorticities. Generally, the positive vorticity is stronger and more active than the negative vorticity. This asymmetry is quantitatively revealed on the basis of a statistical result. The probability density functions (PDFs) of the relative vorticity, and horizontal and vertical velocities at different depths in December 2009 are plotted in Fig. 4. The PDFs of the relative vorticity exhibit a significantly obvious positive skewness near the surface. The negative normalized vorticity is approximately 3 under the probability that the positive normalized vorticity reaches 5, the negative one is just around 3. The corresponding skewness is 1.40. By contrast, the relative vorticity weakens sharply, and the PDF becomes symmetric with a skewness of as low as –0.29 at the depth of 200 m. This asymmetry of the relative vorticity has been reported by different works and attributed to the centrifugal instability (Dong et al., 2007; Capet et al., 2008b; Klein et al., 2008; Lévy et al., 2010; Shcherbina et al., 2013). The centrifugal instability plays a role in dissipating the SMPs when the negative vorticity exceeds the local planetary vorticity. Thus, the centrifugal instability restricts the relative vorticity by $\zeta \geqslant f$.

The PDFs of the horizontal velocities, u and v, also show asymmetry at both depths of 5 and 200 m, respectively, which may be insignificant. Both velocities demonstrate negative a skewness at the depths. The zonal velocity presents a positive skewness of 0.08 at 5 m and 0.02 at 200 m, whereas the meridional velocity has a negative skewness of –0.33 at 5 m and –0.28 at 200 m. During the time for the PDF calculation, there exists an eddy pair as mentioned above (Fig. 3a). The horizontal velocity is enhanced in the junctional area due to the lateral alignment of the eddy pair (Zhang et al., 2016). The southward and eastward currents tend to be enhanced, according to the relative position of the eddy pair. Therefore, the probabilities of strong positive u and negative v are increased, thereby resulting in the positive

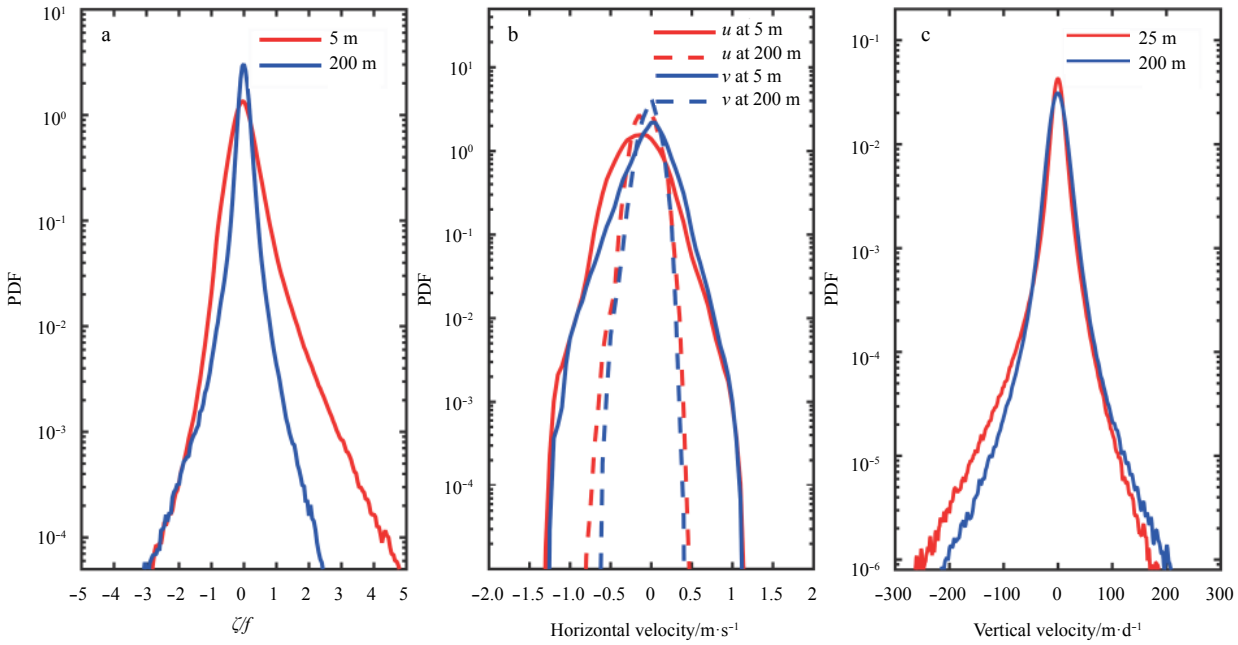

Fig. 4. The probability distribution functions (PDF) of normalized relative vorticity (a), horizontal velocity (b) and vertical velocity (c) at depths of 5 m and 200 m computed based on result in December 2009.

skewness of u and the negative skewness of v.

The PDF of the vertical velocity, w, is asymmetric at the surface with a skewness of approximately –1.70, which indicates that the downwelling is stronger than the upwelling. The downwelling of the vertical velocity can reach 250 m/d. It is stronger than the upwelling which is below 200 m/d. The vertical velocity tends to be symmetric at 200 m depth. On the basis of a simplified vorticity equation, the analysis by Capet et al. (2008b) demonstrated that this asymmetric distribution of the vertical velocity at the surface is consistent with the relative vorticity. Considering that the vorticity variation is only related to the vertical gradient of the vertical velocity, the increasing (decreasing) vorticity strength tends to induce downwelling (upwelling). Accordingly, the dominated positive vorticity at the surface can lead to a dominated downward velocity. This correspondence can be directly observed in Fig. 5. The positive vertical vorticity is stronger at surface, and correspondingly the vertical current is therefore dominated by the downwelling. However, the vertical vorticity at 200 m depth, decreases sharply, thus implying the weakening of submesoscale activity. Though a strong vertical velocity can still be found no consistency is observed between the vertical velocity and the vertical vorticity.

A comparison of the vertical vorticity and velocity indicates that the vertical velocity does not decrease as much as the vertical vorticity, and even the upwelling is stronger at 200 m than at the surface. This inconsistency is attributed to the complicated topography, since strong vertical velocity occurs in the southwest of Taiwan Island and over the shelf break, where there exists complicated topography and strong currents. A strong vertical current can be induced when the flow passes through various topographies.

3.2 *Temporal variation of submesoscale processes*

The above analysis reveals that the SMPs show an asymmetry of the vertical vorticity. The consequent question is that how the SMPs vary in time. The temporal variation features of the SMPs are analyzed from their relative vorticity and kinetic energy.

According to an intuitive expression of the relative vorticity distribution in different seasons, the SMPs seem to be more active in winter than in summer (the distribution figure is not shown). To be more objective and genera, we define the probabilities of the relative vorticity with $|\zeta/f| \geqslant 1$ and the vertical velocity with $|w| \geqslant 50$ m/d as the indicators of the SMP activity. The relative vorticity with $|\zeta/f| \geqslant 1$ and the vertical velocity with $|w| \geqslant 50$ m/d from 2009 to 2012 are calculated (Fig. 6). The probability of $|\zeta/f| \geqslant 1$ at depth of 200 m is low, implying the weakness and inconspicuous variation of the SMPs. However, this probability increases by six to sevenfold and shows an obvious seasonal variation as the depth decreases to 5 m. The probability of the strong vorticity is low in summer (June, July and August) and then increases significantly in winter (December, January and February). Overall, the probability of the strong vorticity is several times higher in winter than in summer.

Meanwhile, the vertical velocity is stronger in winter than in summer as well. The probability of the strong vertical velocity at the surface shows a similar variation feature; this is consistent with the relative vorticity, which has a correlation coefficient of up to 0.72. However, the probability at 200 m does not show a seasonal variation, although the probability density varies with time. In contrast to the relative vorticity variation with the depths, the vertical velocity is stronger at 200 m than that at 25 m. This outcome may be attributed to the rapidly changing topography, as mentioned in the above subsection.

The probabilities of the strong relative vorticity and vertical velocity reveal a strong seasonal variation of the SMPs, thus implying a higher SMP kinetic energy (KE) in winter than in summer. The SMP KE is calculated after the flow decomposition to confirm the above-mentioned result. The velocity field is first decomposed into three components with different spatial scales, as follows:

$$\boldsymbol{u}_{\mathrm{t}}=\boldsymbol{u}_{\mathrm{l}}+\boldsymbol{u}_{\mathrm{m}}+\boldsymbol{u}_{\mathrm{s}}, \tag{1}$$

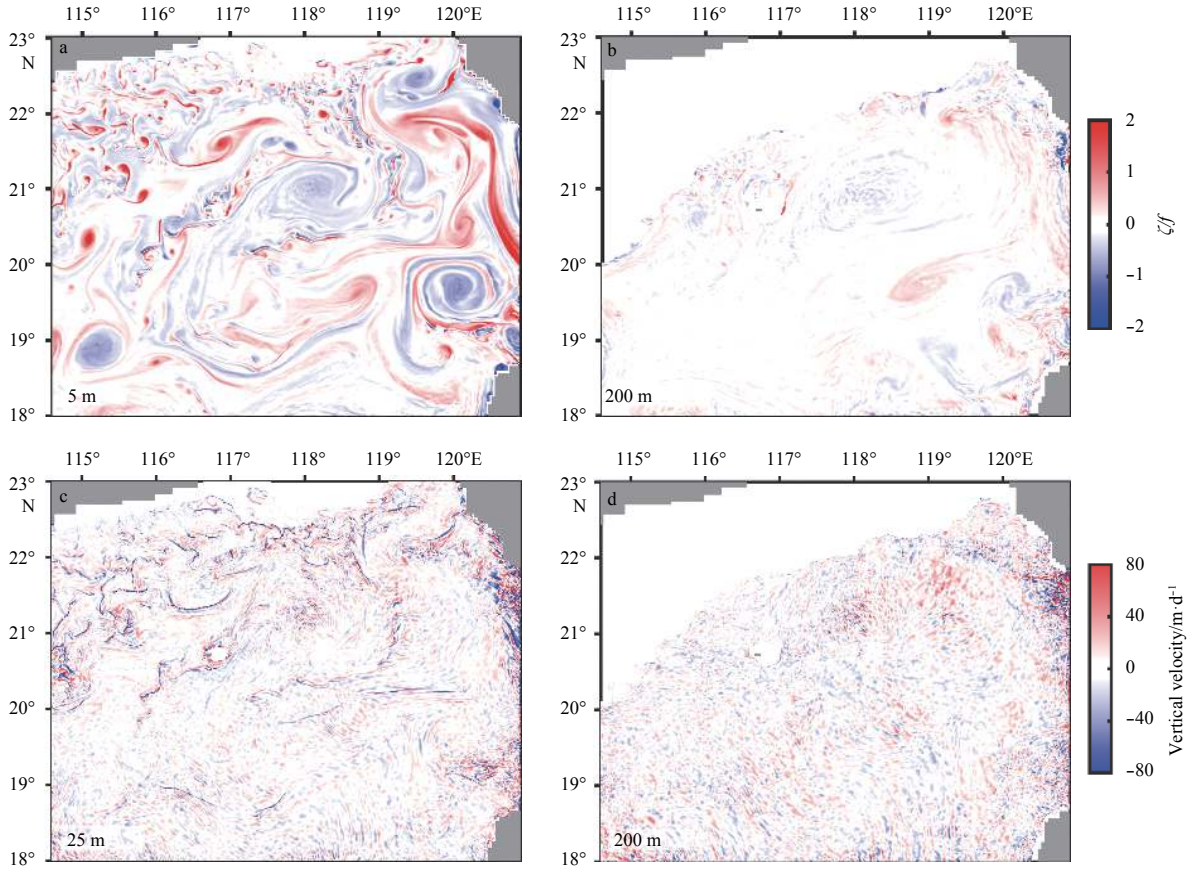

Fig. 5. The normalized relative vorticity (a, b) and vertical velocity (m/d) (c, d) at 5 m (left) and 200 m (right) on December 17, 2009.

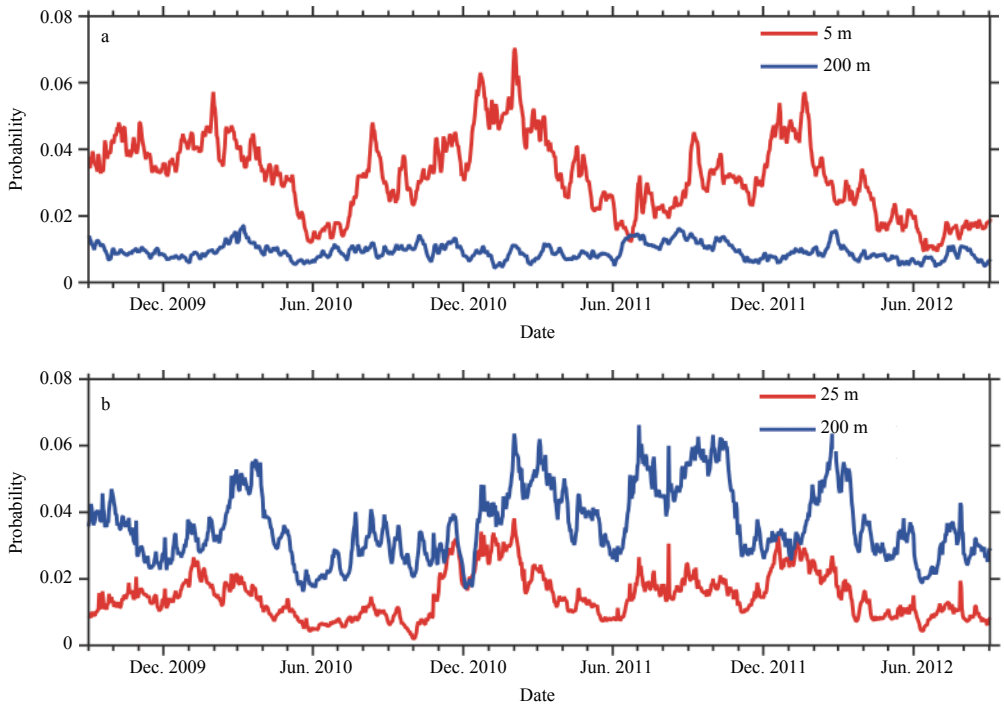

Fig. 6. The time series of probabilities of the normalized relative vorticity in the range of $\{\zeta/f \mid |\zeta/f| \geqslant 1\}$ (a) and vertical velocity in the range of $\{w \mid |w| \geqslant 50$ m/d$\}$ (b). The red lines denote the probabilities at surface (5 m for vorticity, 25 m for vertical velocity), while the blue lines denote the probabilities at 200 m.

where $\boldsymbol{u}_t$ is the total velocity; and $\boldsymbol{u}_l$, $\boldsymbol{u}_m$ and $\boldsymbol{u}_s$ correspond to the large-scale, mesoscale, and submesoscale velocities. The partition scales between different flow fields are selected as follows. Under the baroclinic instability, the disturbance develops at a scale of

$$L = \frac{NH}{f}, \tag{2}$$

where N is the buoyancy frequency; H is the vertical scale of the disturbance; and f is the Coriolis parameter. According to the water depth and the mixed layer depth (MLD), the scales used to partition large- and mesoscales, meso- and submesoscales are defined as 400 and 20 km, respectively. Our evaluation indicates that the Rossby number calculated based on the submesoscale velocity field with the partition scale of 20 km is nearly consistent with the result calculated from the total velocity field. This consistent relationship indicates that the spatial scale used here can extract most submesoscale energy, though it may be not perfect.

The speed fields ($|\boldsymbol{u}_l|$, $|\boldsymbol{u}_m|$ and $|\boldsymbol{u}_s|$) of the different scales at 5 m depth on 17 December, 2009 are calculated as an example (Fig. 7) using the Butterworth filter. The speed field is filtered meridionally and then zonally. The speed patterns depict the large-scale circulation and mesoscale eddies, and demonstrate the SMP activity which is consistent with the relative vorticity. Therefore, the distributions of the different velocities indicate that this method can distinguish the KE of the different scales well.

The KE densities (KE=$\rho\boldsymbol{u}^2/2$) of the different scales at the surface and 200 m depth are calculated and plotted versus time (Fig. 8). Most KE is concentrated in the upper layer, and the large- and mesoscale energies are the dominant components of the oceanic KE. The large- and mesoscale KE near the surface are comparable, with a variation range from about 200 J/m^3 to nearly 600 J/m^3. Both decrease sharply at 200 m depth below 100 J/m^3, with inconspicuous temporal variations. Similarly, the submesoscale energy is much stronger in the upper layer than at 200 m depth. By contrast, the submesoscale energy is much smaller, which accounts for only 2% of those two components. Nevertheless, the kinetic energy of the SMPs exhibits an apparent seasonal variation. It can reach 8 J/m^3 in winter but decreases by half to 4 J/m^3 in summer. This result is consistent with the variation revealed by the relative vorticity and vertical velocity.

3.3 *The generation of submesoscale processes*

As mentioned in Section 1, the SMPs can be generated under different conditions. In the current section, the generation mechanisms are analyzed to determine the reason for the obvious temporal variation of the SMPs. The generation mechanisms that include frontogenesis, MLI are investigated according to their different dynamic features. On the basis of the generation investigation, the potential factors that modulate the seasonal variation of the SMPs are analyzed.

3.3.1 *Frontogenesis*

The frontogenesis is a common mechanism for generating submesoscale fronts in the upper mixed layer (Capet et al., 2008b). The frontogenesis theory reveals that a secondary circulation is induced when the horizontal gradient is strengthened

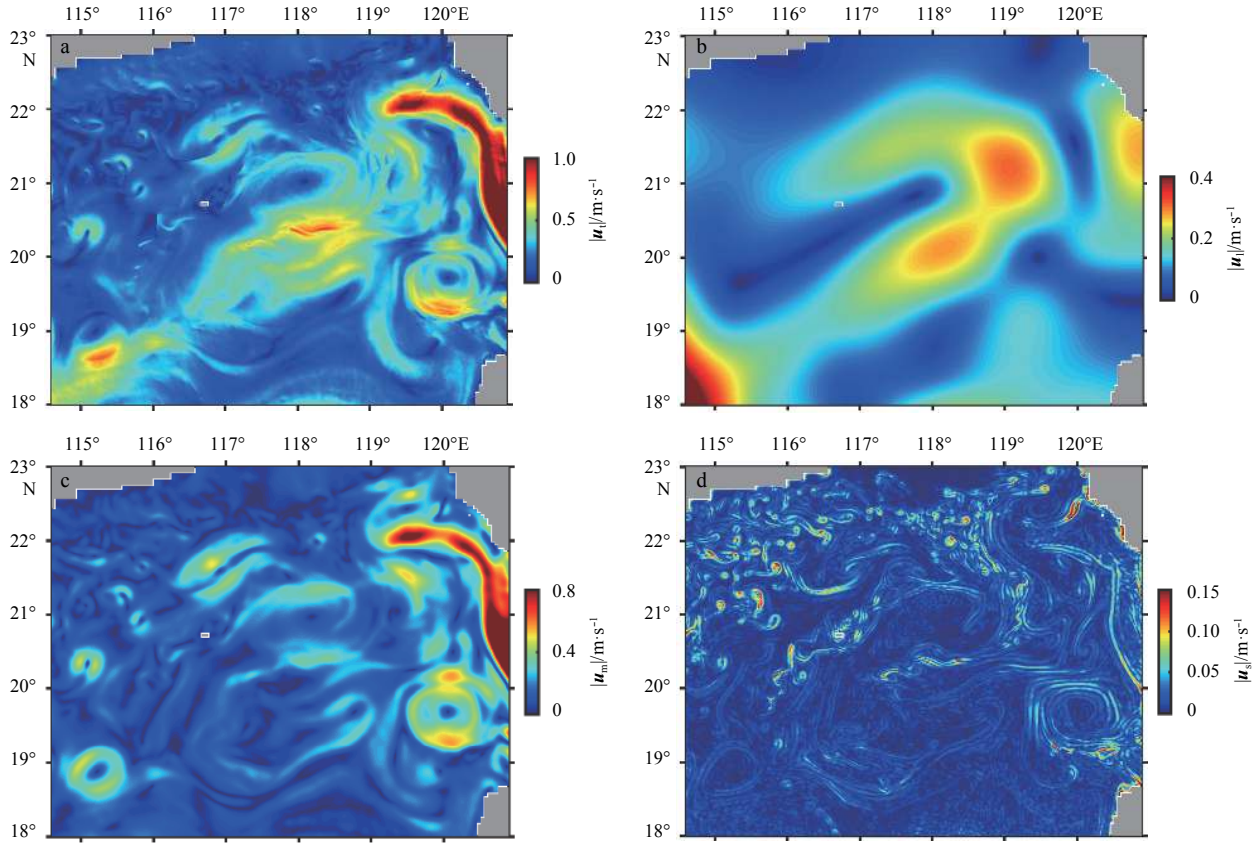

Fig. 7. The total speed $|\boldsymbol{u}_t|$(a), large-scale speed $|\boldsymbol{u}_l|$(b), mesoscale speed $|\boldsymbol{u}_m|$ (c), and submesoscale speed $|\boldsymbol{u}_s|$ (d) on December 17, 2009.

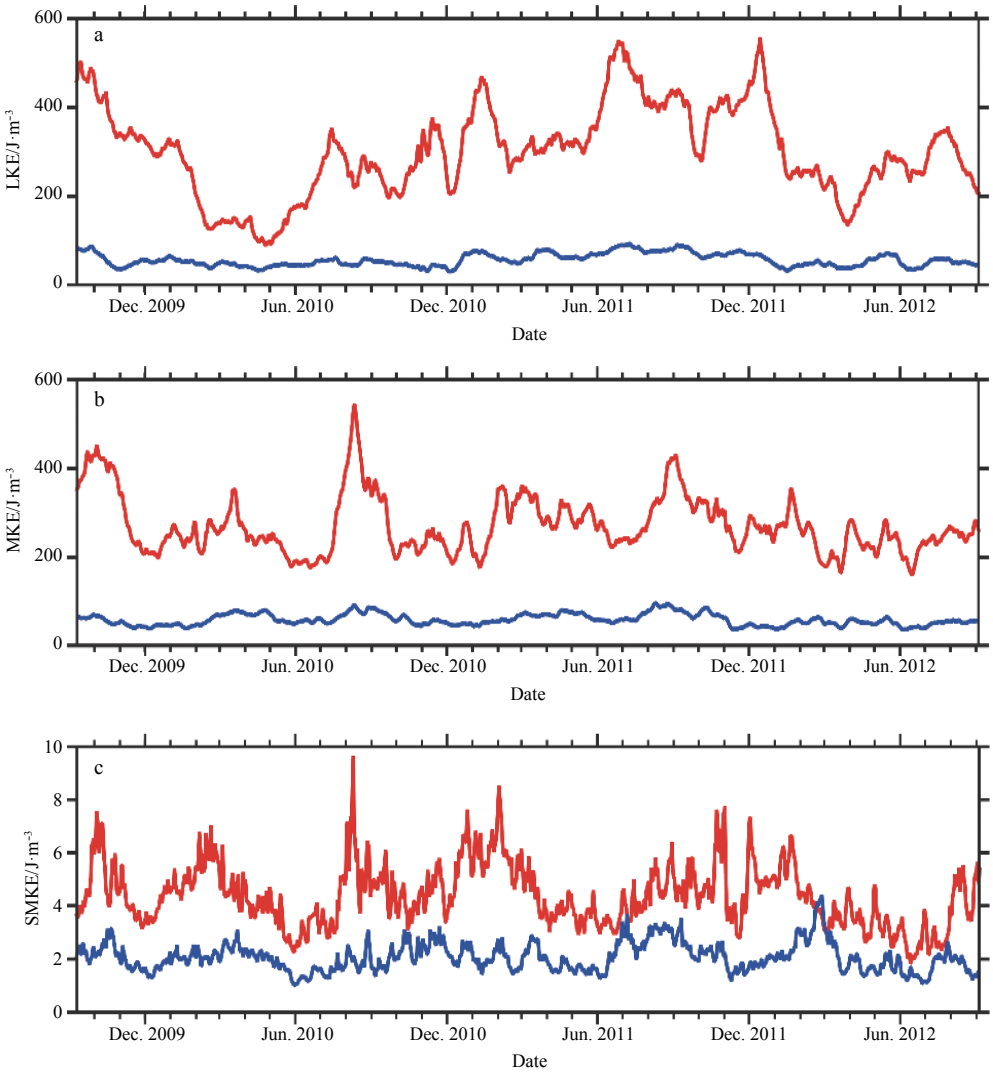

Fig. 8. The time series of large-scale (a), mesoscale (b) and submesoscale (c) kinetic energy density (red lines for series at 5 m, while blue lines for series at 200 m).

continuously (Hoskins, 1982). The induced secondary circulation resists the strengthening of the fronts and restores the geostrophic balance. According to the frontogenesis equation, the frontogenesis is closely related to the straining field of flow (Hoskins, 1982), which can be expressed as

$$S=\sqrt{(u_x-v_y)^2+(u_y+v_x)^2}, \tag{3}$$

where u and v are zonal and meridional velocities, respectively, the parameter S measures the straining rate of the flow. A strong flow straining rate favors the frontogenesis.

According to the calculated results at 5 m on 17 December, 2009 (Fig. 9), the straining field pattern is consistent with the relative vorticity distribution displayed in Fig. 3. The straining fields induced by meso- and submesoscale velocities are comparable and are one order of magnitude larger than those induced by the large-scale velocity. The flow straining causes the frontogenesis on the premise of the horizontal density gradient, which can be depicted by the frontogenesis rate, F (Hoskins, 1982),

$$F=\boldsymbol{Q}\cdot\nabla_{\mathrm{h}}\rho=-\left(u_x\rho_x+v_x\rho_y\right)\rho_x-\left(u_y\rho_x+v_y\rho_y\right)\rho_y. \tag{4}$$

F measures the changing rate of the horizontal gradient induced by the flow straining. The F being greater than 0 indicates an increase of front strength, whereas the front strength decreases when F is less than 0. The frontogenesis rate caused by different velocity fields are calculated, which shows same conclusions with the straining rates. The frontogenesis rate caused by mesoscale and submesoscale velocities remains comparable and is one order larger than that caused by the large-scale velocity (Fig. 10). However, in contrast to the flow straining, the frontogenesis rate has positive and negative values, implying that the flow straining may play a positive role in the generation of the submesoscale fronts, and a negative role in the dissipation of the fronts.

The above-mentioned analysis demonstrates that the flow straining significantly contributes to generating the submesoscale fronts. Therefore, the mesoscale straining and density gradient are important prerequisites during the initial stage of the submesoscale fronts generation. Thus, the probabilities of the strong flow straining, $|S/f|\geqslant 0.8$, and the strong horizontal density gradient, $|\nabla_{\mathrm{h}}\rho|\geqslant 0.05$ kg/km, in mesoscale (the density de-

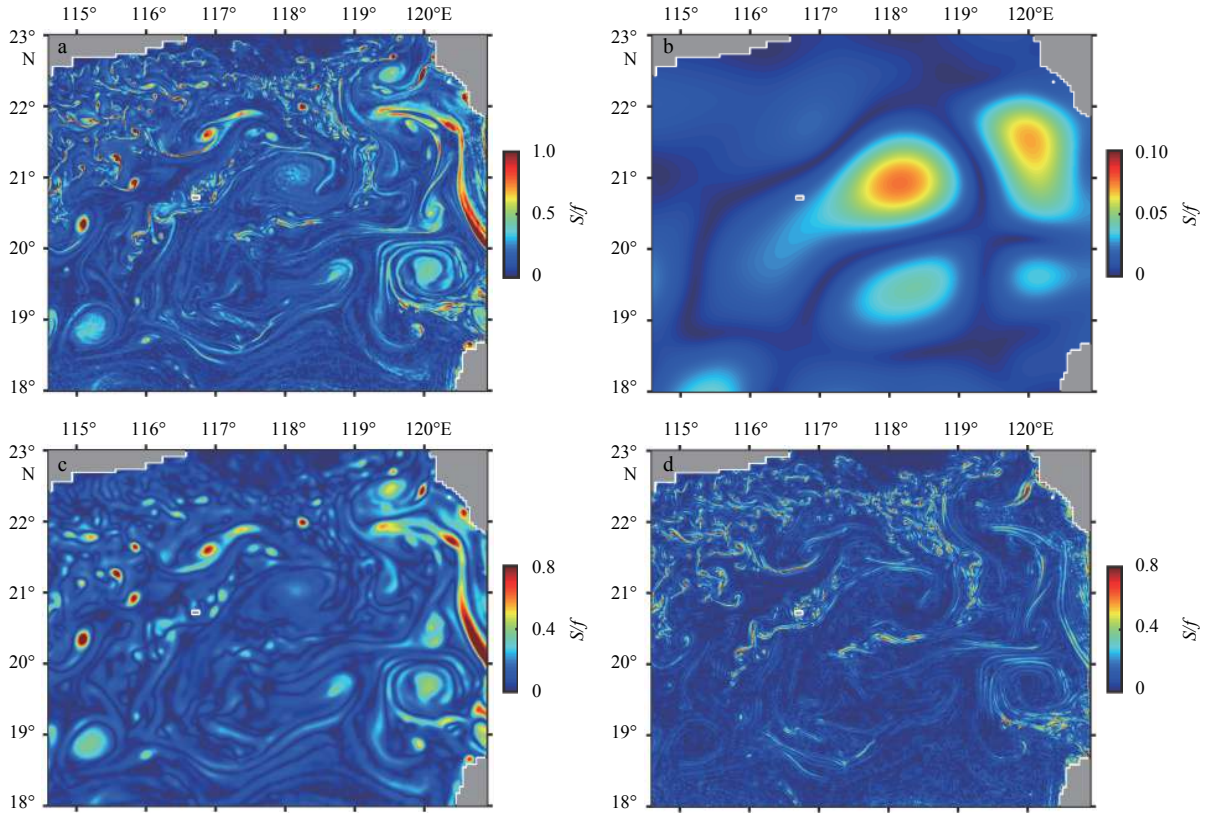

Fig. 9. The straining rates (normalized by f) at 5 m depth induced by total velocity (a), large-scale velocity (b), mesoscale velocity (c) and submesoscale velocity (d) on December 17, 2009.

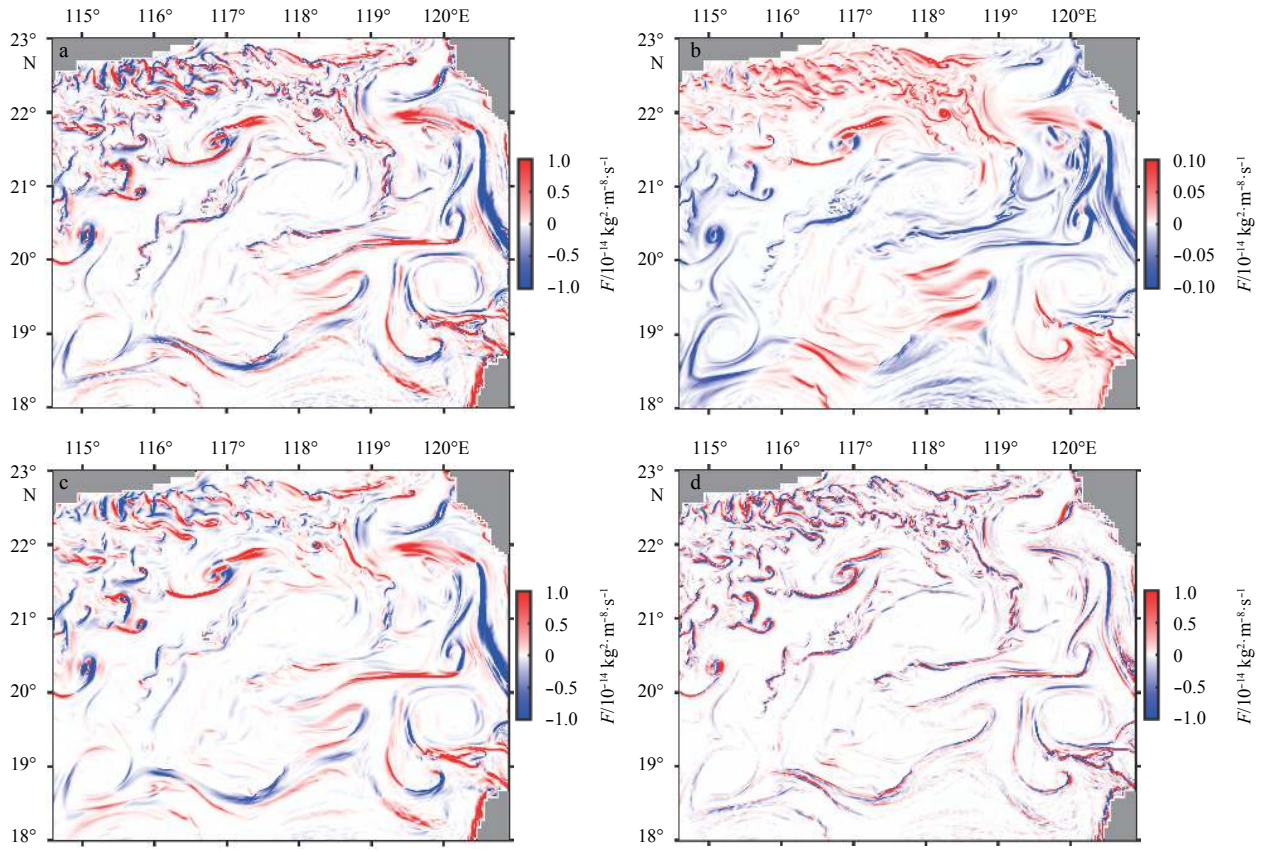

Fig. 10. The frontogenesis rates F (10^{-14} kg^2·m^{-8}·s^{-1}) at 5 m depth induced by total velocity (a), large-scale velocity (b), mesoscale velocity (c) and submesoscale velocity (d) on December 17, 2009.

composition is similar to the velocity decomposition) at different depths are calculated (Figs 11a, b). Both probabilities have a high value at the surface and decrease to nearly 0 at 200 m depth. The strong straining and the density gradient are concentrated in the upper mixed layer, where the strong velocity and the density fluctuation easily appear. Both time series in the upper mixed layer have obvious seasonal variations, which are strong in winter and weak in summer. Given that the strong horizontal density gradient exists in winter, the strong flow straining is potentially in favor of strengthening the front gradients. Therefore, the mesoscale straining and the density gradient are significant factors in modulating the seasonal variation of the SMPs.

Previous studies have revealed that the density gradient variation can be attributed to the seasonal variation of the MLD (Mensa et al., 2013; Callies et al., 2015). The MLD is shallow and tends to be stratified due to the weak summer monsoon while the mixed layer deepens in winter due to the strong winter monsoon. Consequently, the isopycnals easily outcrop and generate the horizontal density gradient in winter. Our analysis reveals that the strong flow straining in winter is another significant factor for modulating the SMPs. In winter, strong Kuroshio intrusions, more active mesoscale eddies and stronger monsoon in the SCS lead to strong straining (Chen et al., 2009; Cheng and Qi, 2010). The *in situ* observations in the SCS have revealed that active SMPs are associated with mesoscale eddies, which play an important role in forward energy cascade (Yang et al., 2017; Zhong et al., 2017). The generation of the SMPs at the periphery of eddies is likely related to the strong staining at the periphery of eddies.

3.3.2 *Mixed layer instabilities*

A careful comparison between the frontogenesis rate and the relative vorticity indicates more fine structures in vorticity, such as more smaller eddies and filaments. The bias suggests that the frontogenesis is not the exclusive mechanism for generating the SMPs. On the basis of the theoretical analysis, Boccaletti et al. (2007) presented that the baroclinic disturbance at the submesoscale grows when the horizontal density gradient and the vertical velocity shear are unstable, namely, MLI. The energy source for MLI is the release of available potential energy (APE), which can be measured by the conversion rate from APE to KE (Boccaletti et al., 2007),

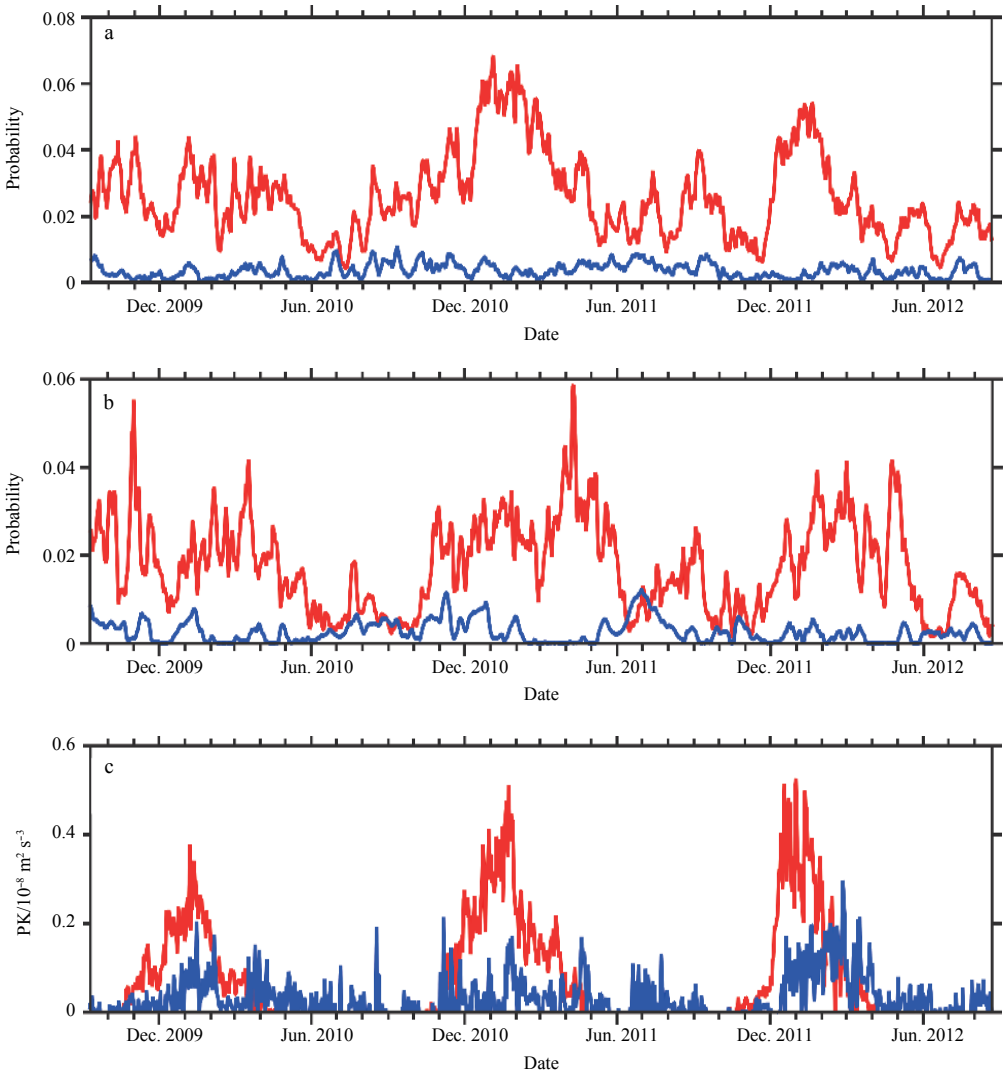

Fig. 11. The time series of probabilities of the straining rate $\{S/f | S/f| \geqslant 0.8\}$ (a), and $\{|\rho_h| \, | \, |\rho_h| \geqslant 0.05$ kg/km$\}$ (red lines for series at 5 m, while blue lines for series at 200 m) (b), and the time series of PK (red lines for series averaged within mixed layer, while blue lines for series averaged between the mixed layer depth and 200 m) (c).

$$\mathrm{PK} = \frac{\int w_s b_s \mathrm{d}v}{\int \mathrm{d}v}, \quad (5)$$

where w_s and b_s are submesoscale perturbations of the vertical velocity and buoyancy, respectively. The PK defined here is a domain-average over different depth ranges. This work investigated the PK averaged within the mixed layer and between the MLD base and 200 m are investigated. The MLD is defined as the depth at which the temperature change from the surface temperature is 0.5℃.

Figure 11c illustrates that the PK is always positive within the calculated depth range, implying a release of the APE to the KE. However, the PK is small below the mixed layer, and little APE is converted to the KE. In the mixed layer, the PK is small in summer but increases sharply in winter, indicating a strong seasonal variation in the APE release. In winter, more APE release provides energy for the development of the SMPs. But in summer, the SMPs can hardly extract the APE in the mixed layer for their development. Therefore, the MLI is another factor for modulating the seasonal variation of the SMPs (Capet et al., 2008c).

The magnitude of the APE is limited by the thickness of the MLD (Mensa et al., 2013). The MLD is shallow in summer but is deepened in winter due to the monsoon variation. The more easily outcropping isopycnals and stronger frontogenesis are in favor of storing more APE within the MLD in winter than that in summer. Meanwhile, stronger mesoscale eddies and monsoon favor density gradient due to the difference of water masses and flow straining, which further increases the APE.

It can be inferred that the frontogenesis and the MLI are tightly related, rather than mutually independent. The pre-existing density gradient is an essential condition for both generation mechanisms. However, the pre-existing density gradient is usually too weak for the MLI. When frontogenesis occurs and front gradients are strengthened, it is usually accompanied by the MLI due to the unstable strong density gradient and velocity shear. So, the flow straining and the MLD are the contributors for both frontogenesis and MLI. Their seasonal variations are the main factors that modulate the SMP seasonal variation.

4 Summary

The SCS is one of the largest marginal seas in the world and has abundant and complicated dynamical processes. As the transitional scale between mesoscale and microscale, the SMPs are ubiquitous in the upper layer of the SCS. The spatiotemporal variation features of the SMPs are analyzed, using a high-resolution model in the northeastern SCS.

The results reveal that the SMPs are mainly concentrated in the upper mixed layer and sharply weaken as depth increases. Owing to the centrifugal instability, the SMPs with negative vorticity in excess of the local planetary vorticity tend to be dissipated rapidly. Thus, the vorticity and the vertical velocity are asymmetric, with corresponding PDF skewness of approximately 1.4 and –1.7. Moreover, the SMPs have an obvious seasonal variation, which is stronger and more active in winter than in summer. According to the estimation, the submesoscale KE can reach 8 J/m^3 in winter, which is two-fold larger than that in summer.

The generation mechanisms of the SMPs play a significant role in modulating the spatiotemporal variation features. On the basis of the frontogenesis theory and the energy conversion rate from APE to KE, we demonstrated that frontogenesis and MLI are important mechanisms for the generation of the SMPs in the upper mixed layer. Further analysis indicates that the strong seasonal variation of the SMPs is attributed to the seasonal variations of flow straining and MLD. The stronger straining and deeper MLD account for the more active SMPs in winter.

References

Alford M H, Peacock T, MacKinnon J A, et al. 2015. The formation and fate of internal waves in the South China Sea. Nature, 521 (7550): 65–69, doi: 10.1038/nature14399

Boccaletti G, Ferrari R, Fox-Kemper B. 2007. Mixed layer instabilities and restratification. Journal of Physical Oceanography, 37(9): 2228–2250, doi: 10.1175/JPO3101.1

Buckingham C E, Naveira Garabato A C, Thompson A F, et al. 2016. Seasonality of submesoscale flows in the ocean surface boundary layer. Geophysical Research Letters, 43(5): 2118–2116, doi: 10.1002/2016GL068009

Callies J, Ferrari R, Klymak J M, et al. 2015. Seasonality in submesoscale turbulence. Nature Communications, 6: 6862, doi: 10.1038/ncomms7862

Capet X, McWilliams J C, Molemaker M J, et al. 2008a. Mesoscale to submesoscale transition in the California current system. Part I: Flow structure, eddy flux, and observational tests. Journal of Physical Oceanography, 38(1): 29–43, doi: 10.1175/2007JPO3671.1

Capet X, McWilliams J C, Molemaker M J, et al. 2008b. Mesoscale to submesoscale transition in the California current system. Part II: Frontal processes. Journal of Physical Oceanography, 38(1): 44–64, doi: 10.1175/2007JPO3672.1

Capet X, McWilliams J C, Molemaker M J, et al. 2008c. Mesoscale to submesoscale transition in the California current system. Part III: Energy balance and flux. Journal of Physical Oceanography, 38(10): 2256–2269, doi: 10.1175/2008JPO3810.1

Chen Gengxin, Hou Yinjun, Chu Xiaoqing. 2011. Mesoscale eddies in the South China Sea: Mean properties, spatiotemporal variability, and impact on thermohaline structure. Journal of Geophysical Research: Oceans, 116(C6): C06018

Chen Gengxin, Hou Yijun, Chu Xiaoqing, et al. 2009. The variability of eddy kinetic energy in the South China Sea deduced from satellite altimeter data. Chinese Journal of Oceanology and Limnology, 27(4): 943–954, doi: 10.1007/s00343-009-9297-6

Cheng Xuhua, Qi Yiquan. 2010. Variations of eddy kinetic energy in the South China Sea. Journal of Oceanography, 66(1): 85–94, doi: 10.1007/s10872-010-0007-y

Dong Changming, Mcwilliams J C, Shchepetkin A F. 2007. Island wakes in deep water. Journal of Physical Oceanography, 37(4): 962–981, doi: 10.1175/JPO3047.1

Gula J, Molemaker M J, McWilliams J C. 2016. Topographic generation of submesoscale centrifugal instability and energy dissipation. Nature Communications, 7: 12811, doi: 10.1038/ncomms12811

Hoskins B J. 1982. The mathematical theory of frontogenesis. Annual Review of Fluid Mechanics, 14(1): 131–151, doi: 10.1146/annurev.fl.14.010182.001023

Huang Xiaodong, Chen Zhaohui, Zhao Wei, et al. 2016. An extreme internal solitary wave event observed in the northern South China Sea. Scientific Reports, 6: 30041, doi: 10.1038/srep30041

Johnson K S, Riser S C, Karl D M. 2010. Nitrate supply from deep to near-surface waters of the north Pacific subtropical gyre. Nature, 465: 1062–1065, doi: 10.1038/nature09170

Klein P, Hua B L, Lapeyre G, et al. 2008. Upper ocean turbulence from high-resolution 3D simulations. Journal of Physical Oceanography, 38(8): 1748–1763, doi: 10.1175/2007JPO3773.1

Lapeyre G, Klein P. 2006. Impact of the small-scale elongated filaments on the oceanic vertical pump. Journal of Marine Research, 64(6): 835–851, doi: 10.1357/002224006779698369

Lévy M, Ferrari R, Franks P J S, et al. 2012. Bringing physics to life at the submesoscale. Geophysical Research Letters, 39(14): L14602

Lévy M, Klein P, Tréguier A M. 2001. Impact of sub-mesoscale physics on production and subduction of phytoplankton in an oligotrophic regime. Journal of Marine Research, 59(4): 535–565, doi: 10.1357/002224001762842181

Lévy M, Klein P, Tréguier A M, et al. 2010. Modifications of gyre circulation by sub-mesoscale physics. Ocean Modelling, 34(1–2):

1–15, doi: 10.1016/j.ocemod.2010.04.001
Liu Q, Kaneko A, Su J. 2008. Recent progress in studies of the South China Sea circulation. Journal of Oceanography, 64(5): 753–762, doi: 10.1007/s10872-008-0063-8
Mahadevan A. 2006. Modeling vertical motion at ocean fronts: are nonhydrostatic effects relevant at submesoscales? Ocean Modelling, 14(3–4): 222–240, doi: 10.1016/j.ocemod.2006.05.005
Mensa J A, Garraffo Z, Griffa A, et al. 2013. Seasonality of the submesoscale dynamics in the gulf stream region. Ocean Dynamics, 63(8): 923–941, doi: 10.1007/s10236-013-0633-1
Nan Feng, Xue Huijie, Xiu Peng, et al. 2011. Oceanic eddy formation and propagation southwest of Taiwan. Journal of Geophysical Research: Oceans, 116(C12): C12045, doi: 10.1029/2011JC007386
Pollard R T, Regier L A. 1992. Vorticity and vertical circulation at an ocean front. Journal of Physical Oceanography, 22(6): 609–625, doi: 10.1175/1520-0485(1992)022<0609:VAVCAA>2.0.CO;2
Rosso I, Hogg A M, Kiss A E, et al. 2015. Topographic influence on submesoscale dynamics in the Southern Ocean. Geophysical Research Letters, 42(4): 1139–1147, doi: 10.1002/2014GL062720
Shcherbina A Y, D'Asaro E A, Lee C M, et al. 2013. Statistics of vertical vorticity, divergence, and strain in a developed submesoscale turbulence field. Geophysical Research Letters, 40(17): 4706–4711, doi: 10.1002/grl.50919
Shchepetkin A F, McWilliams J C. 2005. The regional oceanic modeling system (ROMS): a split-explicit, free-surface, topography-following-coordinate oceanic model. Ocean Modelling, 9(4): 347–404, doi: 10.1016/j.ocemod.2004.08.002
Shu Yeqiang, Xiu Peng, Xue Huijie, et al. 2016. Glider-observed anticyclonic eddy in northern South China Sea. Aquatic Ecosystem Health & Management, 19(3): 233–241
Wang Guihua, Chen Dake, Su Jilan. 2008. Winter eddy genesis in the eastern South China Sea due to orographic wind jets. Journal of Physical Oceanography, 38(3): 726–732, doi: 10.1175/2007JPO3868.1
Xia Changshui, Jung K T, Wang Guansuo, et al. 2016. Case study on the three-dimensional structure of meso-scale eddy in the South China Sea based on a high-resolution model. Acta Oceanologica Sinica, 35(2): 29–38, doi: 10.1007/s13131-016-0805-1
Yang Qingxuan, Zhao Wei, Liang Xinfeng, et al. 2016. Three-dimensional distribution of turbulent mixing in the South China Sea. Journal of Physical Oceanography, 46(3): 769–788, doi: 10.1175/JPO-D-14-0220.1
Yang Qingxuan, Zhao Wei, Liang Xinfeng, et al. 2017. Elevated mixing in the periphery of mesoscale eddies in the South China Sea. Journal of Physical Oceanography, 47(4): 895–907, doi: 10.1175/JPO-D-16-0256.1
Zhang Zhiwei, Tian Jiwei, Qiu Bo, et al. 2016. Observed 3D structure, generation, and dissipation of oceanic mesoscale eddies in the South China Sea. Scientific Reports, 6: 24349, doi: 10.1038/srep24349
Zhang Zhiwei, Zhao Wei, Tian Jiwei, et al. 2013. A mesoscale eddy pair southwest of Taiwan and its influence on deep circulation. Journal of Geophysical Research: Oceans, 118(12): 6479–6494, doi: 10.1002/2013JC008994
Zheng Quanan, Lin Hui, Meng Junmin, et al. 2008. Sub-mesoscale ocean vortex trains in the Luzon Strait. Journal of Geophysical Research: Oceans, 113(C4): C04032
Zhong Yisen, Bracco A, Tian Jiwei, et al. 2017. Observed and simulated submesoscale vertical pump of an anticyclonic eddy in the South China Sea. Scientific Reports, 7: 44011, doi: 10.1038/srep44011
Zu Tingting, Wang Dongxiao, Yan Changxiang, et al. 2013. Evolution of an anticyclonic eddy southwest of Taiwan. Ocean Dynamics, 63(5): 519–531, doi: 10.1007/s10236-013-0612-6